Biomaterials Science

ROYAL SOCIETY OF CHEMISTRY

PAPER

View Article Online
View Journal | View Issue

Check for updates

Cite this: *Biomater. Sci.*, 2025, **13**, 5863

Electrospun PLGA fibers with calcium phosphate nanoparticles: effects of nanoparticle crystallinity and carbonate content on osteogenic activity

Yael del Carmen Suárez-López, [a,b] Reshma Vasantha Ramachandran, [a] Varvara Platania, [c] Nikoleta N. Tavernaraki, [c] Alexandra Teleki, [b] Maria Chatzinikolaidou *[c,d] and Georgios A. Sotiriou *[a,e]

The development of synthetic bone scaffolds that mimic the composition and structure of natural bone remains a critical challenge in regenerative medicine. Calcium phosphate (CaP) nanoparticles, due to their compositional similarity to bone, have shown potential as functional components in bone tissue engineering, yet the influence of their crystallinity and carbonate content on osteogenic activity remains underexplored. In this study, flame spray pyrolysis (FSP) was utilized to synthesize CaP nanoparticles with controlled physicochemical properties, offering a scalable and industrially relevant approach for nanoparticle production. These nanoparticles were incorporated into poly(lactic-*co*-glycolic acid) (PLGA) fibers through electrospinning, forming composite scaffolds. The scaffolds exhibited significant biomineralization in simulated body fluid, promoting hydroxyapatite formation over time, independent of carbonate content or crystallinity. Pre-osteoblastic MC3T3-E1 cell studies demonstrated that the scaffolds supported cell proliferation and differentiation, with crystalline CaP nanoparticles (Ca/P = 2.19) yielding the highest alkaline phosphatase activity and collagen production. These findings highlight the potential of flame-made CaP nanoparticles integrated into electrospun fibers as a promising biomaterial for scalable bone tissue scaffold production.

Received 17th March 2025,
Accepted 25th August 2025

DOI: 10.1039/d5bm00426h

rsc.li/biomaterials-science

Open Access Article. Published on 29 2025. Downloaded on 2025/12/20 04:03:16.
This article is licensed under a Creative Commons Attribution 3.0 Unported Licence.

Introduction

Physiological bone consists of a tridimensional (3D) and porous scaffold made of collagen fibers that are 50 to 500 nm in diameter and have 40 nm gaps between the ends of the molecules, which accommodate hydroxyapatite crystals.[1] Hydroxyapatite is an inorganic crystalline structure composed of carbonated calcium phosphate that provides rigidity and roughness to the bones.[2,3] With more than 2 million grafts done annually in the world, bone is the second most often transplanted tissue in the human body, after blood transfusions.[2] Bone transplants can be done as autografts, where tissue is grafted from the same individual. However, up to 8.6% of patients suffer from donor site complications, such as chronic pain, infections, fractures, or tissue morbidity, and the quantity of tissue that can be grafted is limited.[4,5] An alternative to autografts are allografts, where the tissue is grafted from a different individual other than the patient, usually cadaveric tissue donors. However, there is the risk of immune rejection, potential disease transmission, and slower integration and healing. To address these issues, the development of synthetic materials able to replace natural bone tissue is needed.

Synthetic materials can facilitate cell migration, attachment, and formation of new bone tissue by mimicking the natural bone composition. This would in turn facilitate the integration of the synthetic material to the existing bone, avoid the triggering of adverse immune responses, and match the mechanical properties of the natural tissue. Considering this, recent research has focused on various materials and material structures to develop synthetic alternatives that replicate the structure of natural bone tissue.[6–8]

Calcium phosphate nanoparticles (CaP NPs) resemble natural bone hydroxyapatite. The large surface area of the NPs allows for cells to adhere to the material and aid in adsorption and retention of osteogenic components. Also, the roughness

[a]*Department of Microbiology, Tumor and Cell Biology, Karolinska Institute, 17177 Stockholm, Sweden. E-mail: georgios.sotiriou@su.se*
[b]*Science for Life Laboratory, Department of Pharmacy, Uppsala University, 75123 Uppsala, Sweden*
[c]*Department of Materials Science and Engineering, University of Crete, 70013 Heraklion, Greece. E-mail: mchatzin@materials.uoc.gr*
[d]*Foundation for Research and Technology Hellas-IESL, 70013 Heraklion, Greece*
[e]*Science for Life Laboratory, Department of Chemistry, Stockholm University, 11418 Stockholm, Sweden*

Open Access Article. Published on 29 2025. Downloaded on 2025/12/20 04:03:16.
This article is licensed under a Creative Commons Attribution 3.0 Unported Licence.

and stiffness of the CaP NPs can be sensed by cells, alter cell membrane receptors and trigger mechanotransduction pathways, which in turn influence cell fate toward osteogenesis.[6] CaP NPs also provide calcium and phosphate ion sources that osteoblasts can use for bone metabolism.[6] Dissolution of the calcium and phosphate ions creates a local supersaturation which causes the reprecipitation of biologically carbonated apatite on the scaffold.[9]

Although CaP NPs have gained popularity for these reasons, certain aspects, such as the role of carbonate, remain understudied. Natural hydroxyapatite in the bones has 7% carbonate replacement,[10,11] and the influence of this percentage in synthetic CaP NPs has not been studied. To produce CaP NPs, the sol–gel method is most commonly used. This process generates amorphous CaP NPs,[12] and thus, these NPs are the ones that have been used to investigate osteogenic synthetic materials.[9,13,14] Recently, CaP NPs have been produced by flame spray pyrolysis (FSP), which allows for a fine control of the chemical composition, crystalline structure, and size of the nanoparticles.[15,16] The characteristic fractal nanoaggregate structure in nanoparticles synthesized by FSP enhances the surface-to-volume ratio and may facilitate the nanoparticle–cell interactions and subsequent induction of osteogenic behavior in cells.[7,11] Such interactions depend on the nanotopography of these aggregates, which closely mimic the complex 3D structure of natural bone.[17] Therefore, such a resemblance could enhance cellular interactions and promote bone tissue regeneration. Electrospinning of polymer solutions produces fibers with different diameters that mimic the natural collagen fibers of the bone tissue.[8,18] Poly(lactic-*co*-glycolic acid) (PLGA) is a biocompatible and biodegradable polymer that is FDA approved[19] and can be electrospun into fibers. Furthermore, the mechanical strength of PLGA provides structural integrity to electrospun scaffolds.[19] These attributes make PLGA an excellent material for scaffolding in bone tissue engineering.[20,21]

In this work, the versatility of FSP is exploited to produce CaP NPs with various ranges of crystallinities and carbonate contents. The flame-made CaP NPs were then integrated into PLGA fibers produced by electrospinning to develop scaffolds for bone tissue engineering. The hydroxyapatite formation on these fibers after their incubation in simulated body fluid was examined. Finally, the nanocomposite CaP NPs-PLGA fiber scaffolds were used to grow MC3T3-E1 pre-osteoblastic cells. The outcome of this work will provide the fundamental understanding on the influence of carbonate content and crystallinity of CaP NPs on the osteogenic capacity of the cells.

Materials and methods

Particle synthesis

CaP nanoparticles were produced by flame spray pyrolysis (FSP) as previously described.[16] A liquid precursor solution was prepared by dissolving calcium acetate hydrate (Sigma-Aldrich, Sweden) in a mixture of 1 : 1 propionic acid and 2-ethylhexanoic acid under reflux at 70 °C for 1 h. Then, tributyl phosphate (Sigma-Aldrich, Sweden) was added to yield a solution with a 0.4 M total metal concentration. To obtain calcium phosphate nanoparticles (CaP NPs) with different carbonate content, the nominal ratio of calcium to phosphorus was either Ca/P 2.19 or Ca/P 1.67. To obtain CaP NPs with different crystallinities, the liquid precursor was fed through a capillary and dispersed by oxygen at two different rates, according to Table 1 (where $X : Y$ represents the precursor flow in mL min^{-1} (X) and the dispersion oxygen flow in L min^{-1} (Y)) with a pressure drop at the nozzle of 1.8 bar. The spray was ignited using a pre-mixed methane/oxygen flamelet with flow rates of 1.5 L min^{-1} and 3.2 L min^{-1}, respectively.

Particle characterization

X-ray diffraction (XRD) patterns were collected using a Rigaku MiniFlex 600, CuKα radiation with a 0.02° step and a 2° per min speed and analyzed using PDXL2 software (Rigaku, Germany). Fourier Transform Infrared (FTIR) spectroscopy was performed using a Cary 630 FTIR spectrometer (Agilent, Sweden) with a resolution of 4 cm^{-1} in a 400–4000 cm^{-1} spectral range. The specific surface area (SSA) was determined by the nitrogen adsorption–desorption isotherms (Brunauer–Emmett–Teller (BET) method) in liquid nitrogen at 77 K using a Tristar II Plus (Micromeritics, Norcross, GA, USA) instrument after degassing with N_2 for at least 3 h at 110 °C. The nanoparticle diameter (d_{BET}) in nm was then obtained by using eqn (1).

$$d_{BET} = \frac{6}{\rho \cdot SSA} \quad (1)$$

where ρ is the theoretical density of the sample (3.16 g cm^{-3}) and the SSA is given in m^2 g^{-1}. The CO_3 content of the nanoparticles was calculated by taking the area under the curve (AUC) of the carbonate bands (1350–1450 cm^{-1}) and dividing it by the AUC correspondent to the phosphate stretching (1050–1150 cm^{-1}).[20] Furthermore, additional characterization to quantify the carbonate content based on thermogravimetric analysis (TGA) was carried out.[22] In short, approximately, 85 ± 10 mg of each nanoparticle powder were placed in a platinum pan and analyzed using a TGA550 (TA Instruments, USA) under a nitrogen atmosphere with gas purge of 25 mL min^{-1}. The samples were first heated from room temperature to 150 °C at 20 °C min^{-1} followed by an isothermal period of 30 min to remove moisture. Then, the samples were heated to 550 °C at 20 °C min^{-1} and held at an isothermal period for 30 min to ensure complete combustion of organic matter. Finally, the samples were heated to 950 °C and held for 30 min

Table 1 Conditions used for flame spray pyrolysis

Nanoparticle	10 : 5 Ca/P 2.19	10 : 5 Ca/P 1.67	3 : 8 Ca/P 2.19	3 : 8 Ca/P 1.67
Ca/P ratio	2.19	1.67	2.19	1.67
Precursor rate (mL min^{-1}) (X)	10	10	3	3
Dispersion oxygen rate (mL h^{-1}) (Y)	5	5	8	8

This journal is © The Royal Society of Chemistry 2025

Open Access Article. Published on 29 2025. Downloaded on 2025/12/20 04:03:16.
This article is licensed under a Creative Commons Attribution 3.0 Unported Licence.

to fully decompose carbonates. Eqn (2) was used to calculate the carbonate content:[22]

$$CO_3\% = \frac{(\text{weight at } 550\,^{\circ}\text{C} - \text{weight at } 950\,^{\circ}\text{C})}{\text{weight at } 150\,^{\circ}\text{C}} \times 100 \qquad (2)$$

The samples were suspended in 99.5% ethanol and deposited as a 5 μL drop on a Formvar/Carbon 300 square mesh cupper grid. Then, the particle morphology was visualized by transmission electron microscopy (TEM) with FEI Tecnai G2 Spirit BioTWIN equipment operating at 200 kV and a 2k × 2k Veleta OSiS CCD camera. ImageJ software was used to measure the size of 100 particles. The Sturges method[23] was used to plot histograms and the particle size distributions were determined to be log-normally distributed using the Shapiro–Wilk test for normality and they were then fitted to a log-normal distribution. The primary particle sizes (d_{TEM}) in nm were calculated as the geometric mean and standard deviation from the log-normal curve fitting.

Fiber synthesis

For the fibers that did not contain nanoparticles, Resomer® RG 750 S, poly(D,L-lactide-*co*-glycolide) (PLGA) was purchased from Sigma-Aldrich and dissolved in hexafluoro-2-propanol (HFIP, Sigma-Aldrich, Sweden). The mixture was stirred overnight at room temperature in a glass vial with a magnetic stirrer. For the fibers containing nanoparticles, the flame-made nanoparticles were first dispersed in HFIP at a concentration of 30% w/w based on the later added polymer. For this, the suspension of nanoparticles was first shaken in a FastPrep-24 5G homogenizer (MP Biomedicals, USA) for 1 min with a ceramic ball matrix. Then, 5% w/w (referred to the later added polymer) of Tween20 was added and the shaking was repeated. Then, sonication at 320 W was performed for 30 min and a final sonication step for 5 min at 740 W at 80% amplitude was performed with 10-2s pulse intervals to allow relaxation of the nanoparticles. The nanoparticle suspension was then added to the PLGA polymer and stirred overnight at room temperature in a glass vial with a magnetic stirrer. Other solvent mixtures, chloroform : dimethylformamide in 60 : 40, 50 : 50 and 40 : 60 ratios did not produce fibers or a stable spinning using the described protocol (Fig. S1).

Electrospinning was performed in a Fluidnatek LE-50 (Bioinicia, Spain). All the experiments were performed at room temperature and under 15% humidity. To determine the optimal conditions for fiber electrospinning, a design of experiments (DoE) approach was taken. An Ishikawa diagram (Fig. S2) was used to define the critical process parameters (CPPs) of electrospinning. Failure mode and effects analysis was performed and the variables with a risk priority number higher than 15 were selected for screening experiments using the DoE (Table S1). Screening experiments were used to determine which factors of the electrospinning process had the most significant effects on fiber spinnability and diameter. The experimental design was constructed using MODDE software (version 13, Umetrics AB, Germany) and a D-Optimal design was chosen. Three factors were varied at low, medium, and high levels (Table S2). The polymer concentration was varied at 10, 13, and 15% w/w%, the flow rate of the electrospinning solution was varied at 0.4, 0.8, and 1.2 mL h^{-1}, and the voltage applied was set so that a stable Taylor cone would be produced, and was varied between 4.5 and 7.5 kV. The model fit was evaluated by examining the R^2, Q^2, model validity, and reproducibility. The model was also fine-tuned to improve predictability by removing non-significant model terms ($p > 0.05$), and contour plots were made to visualize the effect of the factors on fiber diameter using MODDE software.

After stable conditions were determined with the DoE, the PLGA polymer concentration was kept at 13% w/w since it allowed for the most stable electrospinning process, the distance of the needle to the collector was kept at 14 cm for all experiments, and the needle was left moving in a transverse path alongside the collector for 8 cm at a rate of 50 mm s^{-1}. For the fibers without nanoparticles, the feeding flow of the polymer was 0.4 mL h^{-1} and the voltage applied was 4.5 kV, while for the fibers containing nanoparticles (NPs), the feeding rate was increased to 0.6 mL h^{-1} and the voltage was increased to 10 kV. The fibers were deposited in a cylindrical rotator (10 cm diameter) covered in aluminum foil. After deposition, the aluminum foil was dismounted for easier handling of the produced fibers.

Fiber characterization

Punched circles of 5 mm were taken from the fibers deposited on the aluminum foil and placed in a metal mount with carbon tape to perform scanning electron microscopy (SEM). SEM micrographs were taken using an Aquilos 2 SEM (Thermo Fisher Scientific, USA). Samples were platinum sputter coated *in situ* with 30 mA current and 1 kV voltage for 15 s before imaging to avoid degradation of the sample. SEM micrographs were taken with a 3 kV beam and dwell time of 1 μs. ImageJ software was used to measure the thickness of 100 different fibers, which then were averaged to report the mean fiber diameter. For transmission electron microscopy (TEM) imaging, the fibers were directly spun on copper grids (200 mesh, Agar Scientific, UK) and imaged using a Talos 120C G2 microscope equipped with a Ceta-D detector and 120 kV LaB_6 source. Prior to imaging, 5 nm of carbon was deposited on the samples using thermal evaporation of a carbon filament in a Leica EMACE600 system to mitigate charging-induced distortion of images.

The mechanical properties of the fibers were analysed with a uniaxial tensile test using a texture analyser (TA.XT plusC, Stable Micro Systems, UK) with the upper grip moving at a speed of 0.02 mm s^{-1}. Fibers were cut into a dog-bone shape (Fig. S3a) ($n = 3$) and Young's modulus was calculated according to the stress–strain curves. Finally, the release of Ca^{2+} from fibers containing CaP nanoparticles was measured. Discs (12 mm in diameter) were cut from the fibers and placed in MilliQ water at 37 °C with stirring for 24 h. The water samples were then sent for calcium analysis using inductively coupled plasma atomic emission spectroscopy (ICP-OES) (Eurofins, Sweden).

Open Access Article. Published on 29 2025. Downloaded on 2025/12/20 04:03:16.
This article is licensed under a Creative Commons Attribution 3.0 Unported Licence.

To determine the number of nanoparticles originally loaded in the fibers, the 12 mm discs were dissolved in HFIP to remove the polymer, and the solution was centrifuged at 22 000*g* for 10 minutes to collect the CaP nanoparticles. These nanoparticles were then dissolved in 2% nitric acid and analyzed by ICP-OES. Calcium release results after 24 h were normalized to the nanoparticle loading in the fibers.

Biomineralization characterization

For each sample of electrospun fibers containing calcium phosphate, 12 mm diameter circles were cut with a punch and hammer. Then, the fiber disks were sterilized in UV for 1 h (30 min on one side and 30 min on the other). Samples were placed separately on wells containing 4 mL of sterile simulated body fluid (SBF) at pH 7.4 and incubated for different intervals (0, 24, and 100 h) at 37 °C. Every 48 h, the SBF was completely replaced by 4 mL of a new sterile SBF to guarantee a constant liquid composition.[15] Each experiment was carried out using 3 disks from the same scaffold. At the end of each time point, the SBF was removed, the disks were washed with MilliQ water, and the samples were left to dry in a hood overnight. After the samples were completely dry, they were placed in a metal mount with carbon tape to obtain SEM micrographs as previously described. In parallel, CaP NP powder in a concentration of 39 mg mL^{-1}, corresponding to the nanoparticles as integrated in the fibers, was dispersed in a sterile SBF and samples were taken at 0, 24, and 100 h intervals. Then, the powder was freeze-dried and XRD diffractograms were recorded as previously described.

Pre-osteoblastic cell culture maintenance and cell seeding

For the viability and morphology evaluation experiments, MC3T3-E1 pre-osteoblastic cells were cultured in alpha-MEM (minimum essential media) (PAN Biotech, Germany), supplemented with 10% FBS (PAN Biotech, Germany), 1% of stock solution penicillin/streptomycin (10.000 U mL^{-1} pen, 10 mg mL^{-1} strep, PAN Biotech, Germany), 1% L-glutamine (PAN-Biotech, Germany) and 1% amphotericin (Gibco, USA). Cells between passages 7 to 11 were used for the experiments. The cell-loaded membranes were maintained under a humidified atmosphere under 5% CO_2 at 37 °C. Culture media were changed every three days. For the osteogenic differentiation experiments, 10 nM dexamethasone, 10 mM β-glycerophosphate, and 50 μg mL^{-1} L-ascorbic acid were added to the primary culture medium.

Cell viability and proliferation assay

The viability and proliferation of MC3T3-E1 pre-osteoblasts cultured in direct contact to the different fibrous scaffolds were quantitatively assessed. The resazurin-based metabolic assay PrestoBlue® (Invitrogen, USA) was conducted as previously described. Briefly, the membranes were cut into circular pieces, with a 10 mm diameter and placed into 48-well plates and each sample was seeded with 2.5×10^4 cells. After 3, 6, and 14 days in culture, the PrestoBlue® reagent was added directly to the wells at a 1 : 10 dilution in a culture medium and incubated at 37 °C for 60 min. The absorbance was measured at 570 and 600 nm using a spectrophotometer (Synergy HT, BioTek, USA). All samples were analyzed in quadruplicate.

Cell morphology *via* SEM

The morphology of MC3T3-E1 pre-osteoblasts seeded onto the fibrous scaffolds was observed using SEM (JEOL JSM-6390 LV), after 3 and 10 days in culture. For the monitoring of osteogenic differentiation of the MC3T3-E1 cells, the mineralization process was observed also *via* SEM, on day 21 of differentiation. Seeded scaffolds with 2.5×10^4 cells per sample for the morphology evaluation and 4×10^4 for the mineralization experiment were placed in a CO_2 incubator at 37 °C. In predetermined time points, samples were removed from the incubator and rinsed three times with phosphate-buffered saline (PBS). Fixation was ensured by submersing the samples in 4% v/v paraformaldehyde for 20 min. Following that, samples were dehydrated in increasing concentrations (30–100% v/v) of ethanol. The cell-seeded fibrous scaffolds were finally dried using hexamethyldisilazane (HMDS), sputter-coated with a 20 nm thick layer of gold (Baltec SCD 050) and observed using a SEM at an accelerating voltage of 15 kV.

Measurement of secreted calcium

Secretion of calcium by cells is considered a late marker for osteogenesis and formation of the bone extracellular matrix. The secreted calcium concentration in culture supernatants has been determined by means of the *O*-cresolphthalein complexone (CPC) method, as previously described.[24] Briefly, a volume of 5 μL of the culture medium from the collected supernatants from each sample type was mixed with 50 μl of calcium buffer and 50 μL of the calcium dye. The solutions were transferred into the wells of a 96-well plate and the absorbance was measured at 570 nm (Synergy HTX Multi-Mode Microplate Reader, BioTek, USA). Samples were analysed in quadruplicate.

Alkaline phosphatase (ALP) activity measurement

Alkaline phosphatase activity was assessed on days 3, 7, and 14. Fibrous scaffolds were seeded with MC3T3-E1 pre-osteoblasts, and underwent thorough washing with PBS and subsequent submerging in 100 μL of lysis buffer (0.1% Triton X-100 in 50 mM Tris-HCl, pH 10.5). After that, samples were subjected to two freeze–thaw cycles, each for 10 min, from −20 °C to room temperature. Then, 100 μL of a 2 mg mL^{-1} *p*-nitrophenyl phosphate (pNPP, Sigma, USA) diluted in 50 mM Tris-HCl at pH 10 with 2 mM $MgCl_2$ were added to each sample and incubated at 37 °C for 60 min. The absorbance was measured at 405 nm using a Synergy HTX plate reader (BioTek, USA) and was correlated to equivalent amounts of *para*-nitrophenol using a calibration curve. The enzymatic activity was calculated using the equation [units = nmol *p*-nitrophenol min^{-1}] and normalized by the total protein. All samples were analyzed in quadruplicate.

Open Access Article. Published on 29 2025. Downloaded on 2025/12/20 04:03:16.
This article is licensed under a Creative Commons Attribution 3.0 Unported Licence.

Determination of the produced extracellular collagen

The Sirius Red assay (Direct red 80, Sigma-Aldrich, USA) was used to measure the total collagen levels secreted from the pre-osteoblastic cells in the culture medium, as previously described.[25] Briefly, at each time point, 25 μL of culture medium was diluted in dd H_2O at a total volume of 100 μL, mixed with 500 μL of 0.1% Sirius Red Dye in 0.5 M acetic acid and incubated for 30 min at room temperature. After centrifugation of the samples at 15 000*g* for 15 min, the pellets were washed with 1 mL of 0.5 M acetic acid in order to remove the non-bound dye. The samples were finally centrifuged at 15 000*g* for 15 min and pellets were dissolved in 500 μL of 0.5 M NaOH. The absorbance was measured at 530 nm using a Synergy HTX plate reader. The absorbance measurements were correlated to the concentration of collagen type I using a calibration curve.

Statistical analysis

All statistical analyses were performed using GraphPad prism software using a two-way ANOVA model with Šidák correction for multiple comparisons. *, **, ***, and **** denotes a *p*-value less than 0.05, 0.01, 0.001, and 0.0001, respectively.

Results and discussion

CaP NPs with different physicochemical properties were produced by flame spray pyrolysis by tuning the flame parameters (precursor flow rate in mL min^{-1}: oxygen dispersion gas flow rate in L min^{-1}) as well as the Ca/P ratio in the liquid precursor solution (Fig. 1a). Fig. 1b depicts the X-ray diffraction (XRD) patterns of these particles. The precursor : dispersion O_2 ratio of 10 : 5 produced crystalline nanoparticles with peaks that correspond to a hydroxyapatite phase, while a 3 : 8 ratio produced amorphous nanoparticles.[16] A high precursor : dispersion O_2 ratio results in larger particle sizes with higher crystallinity than particles made with lower ratios due to a long residence time of the nanoparticles at high temperatures.[26] Additionally, the nanoparticle crystallinity increased with the Ca/P ratio in both cases.

The crystalline CaP NPs (10 : 5 flame conditions for both Ca/P ratios), were more than twice the size (measured by Brunauer–Emmett–Teller nitrogen adsorption–desorption isotherms, d_{BET}) of those produced by a smaller flame (3 : 8 flame conditions) and had a well-defined spherical morphology (Fig. S4a and b). The more amorphous nanoparticles (3 : 8 flame conditions) were smaller and exhibited a less spherical, more irregular morphology (Fig. S4c and d). While the 3 : 8 flame produced nanoparticles that were smaller in size and more amorphous, these characteristics were not detrimental to their quality. The produced nanoparticles were not perfectly spherical due to the rapid cooling and shorter sintering time inherent in the smaller flame process. The less round shape was a morphological outcome of the controlled synthesis condition that yielded a product exhibiting the desired crystalline and chemical characteristics. These results agreed with the literature in which flame-made crystalline CaP with Ca/P 1.61, 2.19, and 1.7 ratios resulted in 48, 38, and 21 nm (d_{BET}), respectively.[27,28]

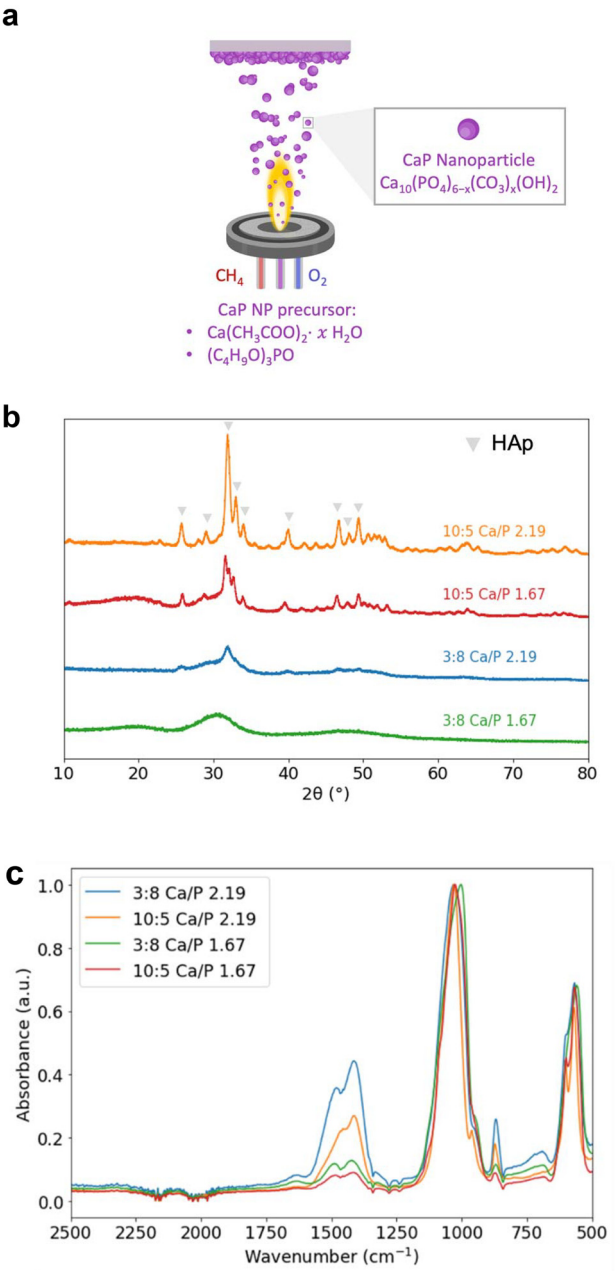

Fig. 1 (a) Schematic representation of FSP production of CaP NPs. (b) XRD patterns and (c) FTIR spectra of the produced nanoparticles.

Fig. 1c shows the Fourier Transform Infrared Spectroscopy (FTIR) spectra of the CaP NPs. The main peaks in FTIR at 550–606 cm^{-1} and 960–1080 cm^{-1} correspond to the phosphate bending and stretching, respectively, while the bands around 1400 cm^{-1} indicate the presence of CO_3.[29] For the amorphous CaP NPs (3 : 8 flame), a reduction in the Ca/P ratio led to a decrease in CO_3 content (Table 2), similar to the observations in more crystalline phases (10 : 5 flame).[29]

Open Access Article. Published on 29 2025. Downloaded on 2025/12/20 04:03:16.
This article is licensed under a Creative Commons Attribution 3.0 Unported Licence.

Table 2 CO_3 content, d_{BET} and d_{TEM} of the samples

Nanoparticle	d_{BET} (nm)	d_{TEM} (nm)	CO_3/P ratio	TGA (CO_3%)
10 : 5 Ca/P 2.19	22.9 ± 0.09	20.8 ± 1.5	0.506	7.3
10 : 5 Ca/P 1.67	24 ± 0.2	23.6 ± 1.5	0.127	0.6
3 : 8 Ca/P 2.19	8.6 ± 0.01	N/A	0.711	7.6
3 : 8 Ca/P 1.67	11.2 ± 0.04	N/A	0.169	0.7

Furthermore, the amorphous nanoparticles exhibited a higher CO_3 content than their crystalline counterparts with the same Ca/P ratio (Fig. 1c and Table 2). Controlling the carbonate content in flame-made CaP NPs allows for a systematic investigation of its effect in biomineralization, as it has been suggested that it plays a crucial role.[30–32] Table 2 details the CO_3/P ratio calculated by the area below the CO_3 and the P bands for each type of nanoparticle, and the CO_3% by thermogravimetric analysis,[22] as well as the nanoparticle diameter (d_{BET} and d_{TEM}).

The electrospinning conditions that produced the most stable fibers without nanoparticles were assessed by a Design-of-Experiments (DoE) approach. A risk assessment through an Ishikawa diagram was constructed to identify variables that may influence critical quality attributes (Fig. S2a) and critical process parameters (Fig. S2b), ultimately impacting the electrospinning process and fibers in bone tissue engineering. Afterwards, the variables were ranked on severity, occurrence, and detectability using failure mode and effects analysis (Table S1). The polymer flow rate, polymer concentration, and voltage applied are known to influence fiber thickness during

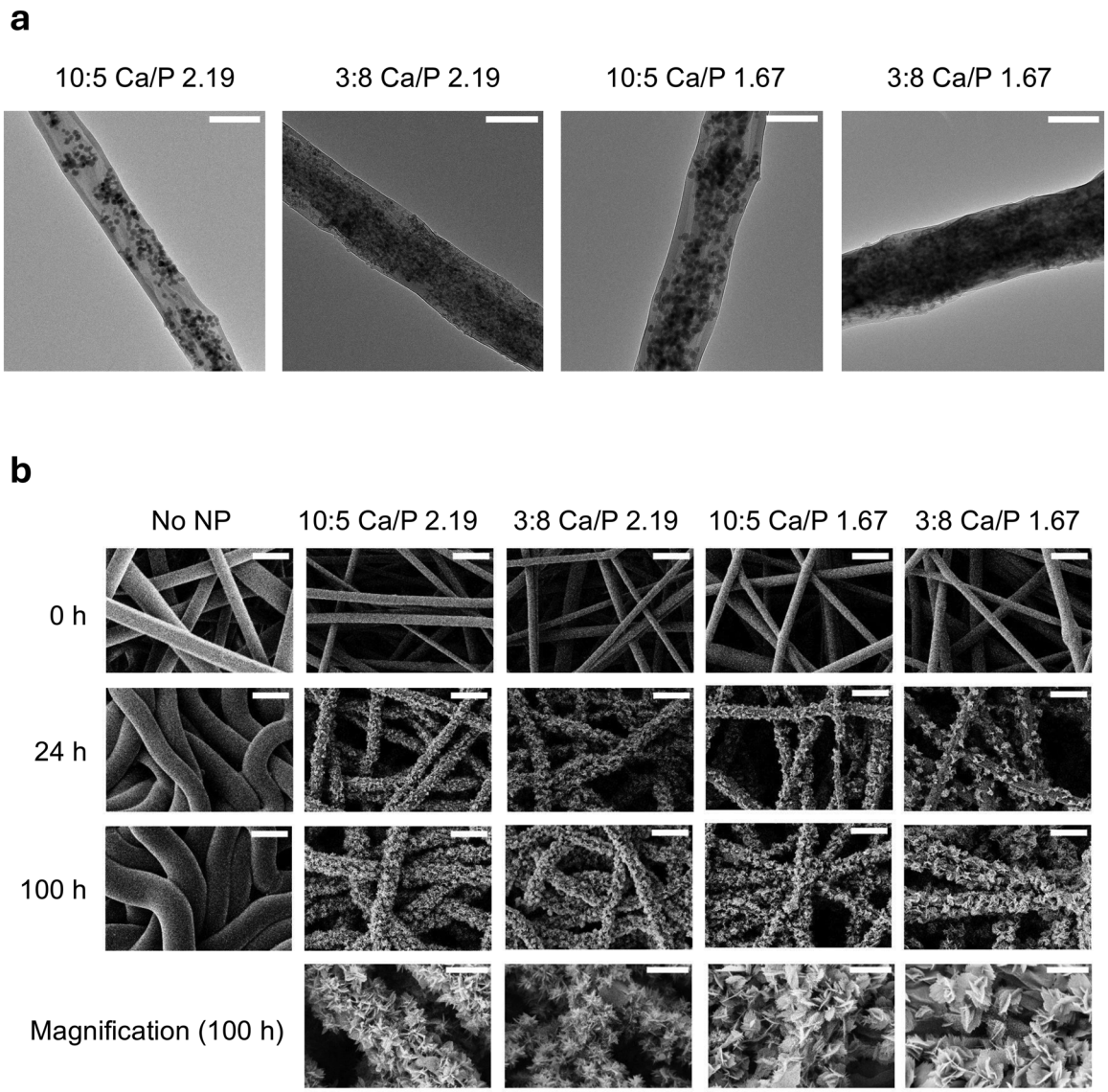

Fig. 2 (a) TEM micrographs of the fibers containing CaP NPs. Scale bar is 200 nm. (b) SEM micrographs of the fibers incubated in SBF for 24 and 100 h. Scale bar is 3 μm, except for the magnified micrographs, where the scale bar corresponds to 1 μm.

 This journal is © The Royal Society of Chemistry 2025

Open Access Article. Published on 29 2025. Downloaded on 2025/12/20 04:03:16.
This article is licensed under a Creative Commons Attribution 3.0 Unported Licence.

the electrospinning process,[33,34] so they were ranked with a high-risk priority number (>15). A DoE (Table S2) was constructed to link and quantify the effect of electrospinning parameters on the fiber thickness using a D-optimal design. Since the voltage influences fiber thickness and the stability of the Taylor cone, the voltage needed to be adjusted in each experiment to ensure a stable electrospinning process. Multiple linear regression was used to model the fiber thickness (Table S3). The adjusted model resulted in a good fit for fiber thickness (R^2 = 0.93 and Q^2 = 0.80). Electrospinning parameters affected the fiber thickness, with the polymer concentration having the strongest positive influence (Fig. S5). As the polymer concentration and polymer flow rate increase, the fiber thickness increases as well, which was in accordance with the previous studies.[34] Polymer concentration was chosen to be at 13% w/w since it was observed that the most stable electrospinning process was obtained at this level, and a flow rate of 0.4 mL h^{-1} was also chosen since thinner electrospun fibers are generally preferred for growing cells.[35]

Fibers containing 30% w/w CaP NPs relative to PLGA were prepared *via* electrospinning and flow and voltage were adjusted to achieve a stable Taylor cone. Proper dispersion of nanoparticles in the solvent before adding the polymer was necessary to ensure their integration into the fibers and to prevent aggregation and needle clogging. For this, nanoparticles were first shaken in a tissue homogenizer, treated with Tween 20, and subjected to sequential sonication at 320 W for 30 min and 740 W for 5 min with 9 : 1 s pulses. Scanning electron microscopy of 5 mm punched circles from the fibers revealed that all samples had a fiber thickness between 0.6 and 1.5 μm (Fig. S6 and Table S4). For fibers without nanoparticles, higher voltages failed to produce a stable Taylor cone, resulting in thicker fibers due to the lower applied voltage. A polymer flow of 0.4 mL h^{-1} was necessary to achieve a stable Taylor cone. Fibers containing nanoparticles had diameters between 700 and 800 nm and exhibited a rough surface, attributed to the presence of nanoparticles, while fibers without nanoparticles had a smooth surface (Fig. S6). Electrospun fibrous membranes have been reported as attractive flexible scaffolds for the regeneration of flat bone defects.[36]

The measurement of Young's modulus showed that fibers with a 1.67 Ca/P ratio were stiffer than those with a 2.19 ratio (Fig. S3b), with the highest stiffness observed for the 10 : 5 flame condition 1.67 Ca/P ratio (0.80 ± 0.03 MPa) and the lowest for the 3 : 8 flame condition 2.19 Ca/P ratio (0.54 ± 0.01 MPa). For both Ca/P ratios, the 10 : 5 flame condition produced higher moduli than the 3 : 8 flame. Considering that the 10 : 5 flame condition produced bigger nanoparticles, this suggests that the number of loaded nanoparticles influences fiber microstructure and stiffness.[37] However, Young's moduli for all the scaffolds were in the range of 0.5 to 0.8 MPa. Signalling *via* integrin pathways were triggered at stiffness values above tens of kPa, with higher stiffness strengthening these cues.[38,39] These mechanotransduction pathways could drive osteogenesis, indicating that the stiffness values of the scaffolds were in a conducive range to support osteogenic differentiation.

Transmission electron microscopy (TEM) micrographs of the CaP NP containing fibers are presented in Fig. 2a. Uniform distribution of the particles could be observed in all fibers, with the nanoparticles produced at bigger flames (10 : 5) appearing larger than the particles produced at a smaller (3 : 8) flame, in accordance with Fig. S4 as well. Ca^{2+} release was within 0.1–0.7% for all fiber samples (Fig. S7). Fig. 2b presents scanning electron microscopy (SEM) images from the biomineralization experiments at various time points, showing sig-

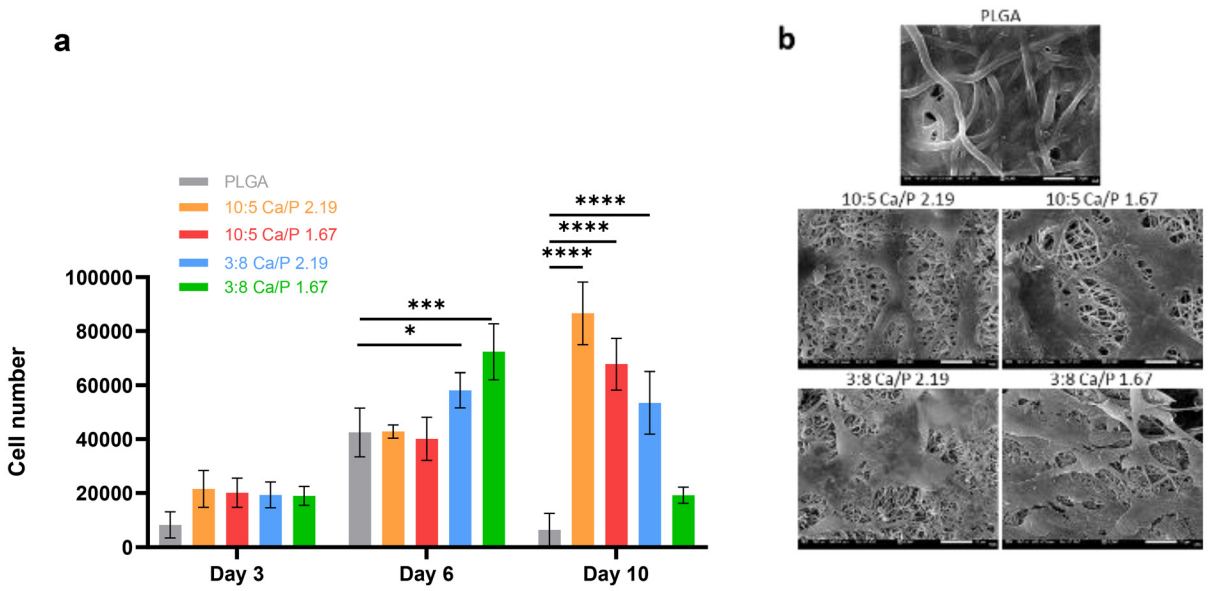

Fig. 3 (a) Cell viability of MC3T3-E1 cells after 3, 6, and 10 days of incubation with PLGA fibers incorporated with flame-made calcium phosphate nanoparticles. (b) Cell morphology after 6 days in culture.

Open Access Article. Published on 29 2025. Downloaded on 2025/12/20 04:03:16.
This article is licensed under a Creative Commons Attribution 3.0 Unported Licence.

nificant CaP crystal deposition on the fibers, which increases with incubation time. Ca^{2+} release ranged from 0.1% to 0.7% across all fiber samples. The slight variations may be related to fiber thickness, as the 10 : 5 Ca/P ratio 2.19 sample also contained the thinnest fibers (Fig. S6 and Table S4). XRD analysis of SBF-incubated CaP NPs revealed a trend towards a hydroxyapatite crystalline phase, regardless of the initial crystallinity of the nanoparticles (Fig. S8). These observations indicated that hydroxyapatite deposition on fibers significantly increased over time, with longer incubation periods enhancing this effect. These results could be attributed to the role of CaP nanomaterials as sources of Ca^{2+} and PO_4^{3-} ions.[9] The release of Ca^{2+}, PO_4^{3-}, and HPO_4 ions into the surrounding tissue leads to local supersaturation, promoting hydroxyapatite reprecipitation on the scaffold.[9,15] In solution, initial hydroxyapatite precipitation from CaP materials forms spherulites composed of radially oriented platelet crystallites. The carbonate content and initial crystallinity of the samples did not affect scaffold bioactivity, as hydroxyapatite crystals continued to grow over time in all four samples (Fig. 2).

The cytotoxicity of fibers incorporated with CaP NPs was determined by the PrestoBlue™ viability assay using the mouse calvaria-derived pre-osteoblastic cells MC3T3-E1.[40] Cell morphology was visualized *via* SEM. Fig. 3a and b show the viability after 3, 6, and 10 days of incubation with the fibers, as well as their morphology on day 6. The values on day 10

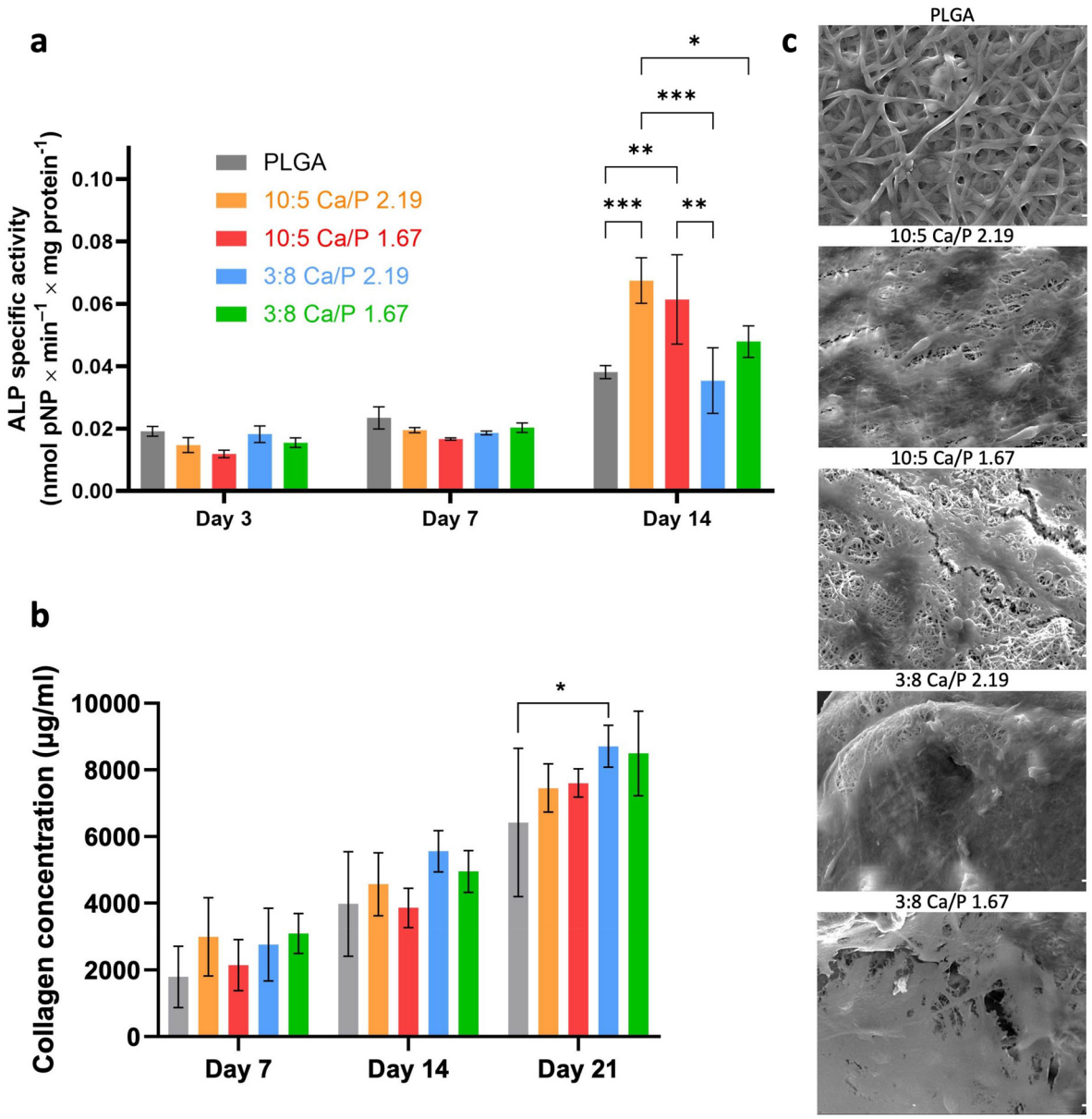

Fig. 4 (a) ALP activity and (b) collagen production of MC3T3-E1 cells in osteogenic media after 3, 7, and 14 days of incubation with PLGA fibers incorporated with flame-made calcium phosphate nanoparticles. (c) Cell morphology on fibrous scaffolds after 14 days.

This journal is © The Royal Society of Chemistry 2025

Open Access Article. Published on 29 2025. Downloaded on 2025/12/20 04:03:16.
This article is licensed under a Creative Commons Attribution 3.0 Unported Licence.

showed that the fibers supported cell proliferation, with those containing crystalline CaP NPs (10 : 5 Ca/P 2.19) providing the most favourable environment. These observations were corroborated by the characteristic elongated cell morphology on day 6, across all five matrices, suggesting the absence of cytotoxic effects up to day 10 (Fig. S9). The cell layer density was higher for fibers with crystalline CaP NPs; however, cells reached confluence earlier on samples with amorphous particles (3 : 8 Ca/P 2.19 and 3 : 8 Ca/P 1.67), which may explain the observed decrease in cell proliferation on day 10 on these fibers, as shown in Fig. 3a. Thus, the cytocompatibility assessment revealed that fibers embedded with CaP NPs provided an optimal environment for the proliferation of pre-osteoblastic cells, with crystalline NPs being the preferred formulation.

The osteogenic potential of the fibers was evaluated by measuring ALP and collagen formation, both of which are indicative of the differentiation of pre-osteoblastic MC3T3-E1 cells into mature osteoblasts.[41,42] Additionally, a cresolphthalein complexone (CPC) assay was performed to directly quantify soluble calcium secreted by the MC3T3-E1 cells (Fig. S10). The CPC assay showed that all groups increased calcium production over 21 days. Variations in the Ca/P ratio or flame conditions had a minimal effect on the calcium production, with all Ca/P groups performing similarly (Fig. S10). Cell morphology was observed *via* SEM. Fig. 4a, b and c illustrate the ALP activity, the produced collagen following 3, 7, and 14 days of incubation on the fibrous scaffolds, and cell morphology on day 14. The ALP activity peaked on day 14 in fibers containing crystalline CaP NPs (10 : 5 Ca/P 2.19), while collagen formation remained consistent across different matrices and exceeded that in blank PLGA fibers. This finding aligns with the literature where ALP activity is low in pre-osteoblasts but increases in immature and mature-osteoblast stages, whereas collagen type I is expressed in pre-, immature- and mature-osteoblast stages.[42]

Scanning electron microscopy images further support these findings, showing clear signs of cell maturation by day 21 (Fig. S11). Additionally, mature osteoblasts formed clusters and aggregates as they produce and deposit bone matrix, which were observed in the images as denser areas of cells with a higher concentration of extracellular matrix material. Notably, ALP activity and SEM images suggest that this differentiation occurs more rapidly on fibers integrated with crystalline CaP NPs. Thus, fibers containing crystalline CaP NPs created the most favourable environment for osteogenesis, likely due to their hydroxyapatite phase, which is similar to the inorganic component of bones and possesses osteoinductive potential.[43,44]

Prior research has shown that hydroxyapatite (HAP)-like crystalline CaP structures provide superior osteoinductive properties compared to amorphous calcium phosphate (ACP). For instance, Hu *et al.*[45] demonstrated that well-crystallized HAP nanoparticles promoted mesenchymal stem cell adhesion, proliferation, and differentiation more effectively than amorphous CaP nanoparticles. Similarly, ter Brugge *et al.*[46] investigated the effect of CaP coating crystallinity on rat bone marrow stem cell differentiation. They found that crystalline CaP coatings stimulated cell differentiation to a greater extent than amorphous coatings, which exhibited negative effects on cell growth and differentiation. The findings of this study were in line with these observations, showing that crystalline CaP nanoparticles enhance osteogenic differentiation, likely due to their structural similarity to the inorganic phase of bones.

Conclusions

This study advances the understanding of how calcium phosphate (CaP) nanoparticle crystallinity and carbonate content influence biomineralization and osteogenic cell responses in electrospun poly(lactic-*co*-glycolic acid) (PLGA) scaffolds. By leveraging flame spray pyrolysis (FSP), the ability to control nanoparticle physicochemical properties in a scalable and industrially relevant manner was demonstrated. The integration of these nanoparticles into electrospun fibers resulted in composite scaffolds that successfully promoted hydroxyapatite deposition and supported osteogenic differentiation of pre-osteoblastic MC3T3-E1 cells. Neither the carbonate content nor the crystallinity affected the biomineralization of the developed scaffolds. However, scaffolds containing crystalline CaP nanoparticles (Ca/P = 2.19) exhibited the highest alkaline phosphatase activity and collagen production, highlighting the role of nanoparticle crystallinity in enhancing osteogenesis. These findings provide fundamental insights into the design of bioactive scaffolds for bone tissue engineering and underscore the potential of FSP-derived CaP nanoparticles for industrial-scale applications. Future work should focus on further optimizing the scaffold architecture for enhanced mechanical performance and exploring *in vivo* applications to validate the clinical potential of these biomaterials. Expanding this research could pave the way for next-generation bone graft substitutes that more closely mimic the complexity of natural bone regeneration.

Conflicts of interest

There are no conflicts of interest to declare.

Data availability

Data for this article, including raw data, are available at Karolinska Institutet's Electronic Notebook platform at eln.ki.se.

Supplementary information is available. See DOI: **https://doi.org/10.1039/d5bm00426h**.

Acknowledgements

This work received funding from the European Research Council (ERC) under the European Union's Horizon 2020 Research And Innovation Program (ERC Grant Agreements

758705 and 101002582). Funding from the Karolinska Institutet, the Swedish Foundation for Strategic Research (SSF) (FFL18-0043), the Swedish Research Council (No. 2024-06173 and 2023-03057), the Strategic Research Area in Stem Cells and Regenerative Medicine (KI) and the Hellenic Foundation for Research and Innovation (grant number: HFRI-FM17-1999) is acknowledged. The Science for Life Laboratory is also gratefully acknowledged for financial support. The Karolinska Institutet 3D-EM facility is kindly acknowledged for the use of their equipment.

Open Access Article. Published on 29 2025. Downloaded on 2025/12/20 04:03:16.
This article is licensed under a Creative Commons Attribution 3.0 Unported Licence.

References

1 S. V. Dorozhkin, Nanosized and nanocrystalline calcium orthophosphates, *Acta Biomater.*, 2010, **6**, 715–734.
2 R. J. Miron, Optimized bone grafting, *Periodontol*, 2024, **94**, 143–160.
3 B. S. Noble, The osteocyte lineage, *Arch. Biochem. Biophys.*, 2008, **473**, 106–111.
4 F. Migliorini, F. Cuozzo, E. Torsiello, F. Spiezia, F. Oliva and N. Maffulli, Autologous Bone Grafting in Trauma and Orthopaedic Surgery: An Evidence-Based Narrative Review, *J. Clin. Med.*, 2021, **10**, 4347.
5 E. D. Arrington, W. J. Smith, H. G. Chambers, A. L. Bucknell and N. A. Davino, Complications of Iliac Crest Bone Graft Harvesting, *Clin. Orthop. Relat. Res.*, 1996, **329**, 300–309.
6 P. Wang, L. Zhao, J. Liu, M. D. Weir, X. Zhou and H. H. K. Xu, Bone tissue engineering via nanostructured calcium phosphate biomaterials and stem cells, *Bone Res.*, 2014, **2**, 14017.
7 Y. He, M. Tian, X. Li, J. Hou, S. Chen, G. Yang, X. Liu and S. Zhou, A Hierarchical-Structured Mineralized Nanofiber Scaffold with Osteoimmunomodulatory and Osteoinductive Functions for Enhanced Alveolar Bone Regeneration, *Adv. Healthc. Mater.*, 2021, **11**, 2102236.
8 O. D. Schneider, S. Loher, T. J. Brunner, L. Uebersax, M. Simonet, R. N. Grass, H. P. Merkle and W. J. Stark, Cotton wool-like nanocomposite biomaterials prepared by electrospinning: In vitro bioactivity and osteogenic differentiation of human mesenchymal stem cells, *J. Biomed. Mater. Res., Part B*, 2008, **84**, 350–362.
9 A. Lotsari, A. K. Rajasekharan, M. Halvarsson and M. Andersson, Transformation of amorphous calcium phosphate to bone-like apatite, *Nat. Commun.*, 2018, **9**, 4170.
10 H. Madupalli, B. Pavan and M. M. J. Tecklenburg, Carbonate substitution in the mineral component of bone: Discriminating the structural changes, simultaneously imposed by carbonate in A and B sites of apatite, *J. Solid State Chem.*, 2017, **255**, 27–35.
11 W. H. Yang, X. F. Xi, J. F. Li and K. Y. Cai, Comparison of crystal structure between carbonated hydroxyapatite and natural bone apatite with theoretical calculation, *Asian – J. Chem.*, 2013, **25**, 3673–3678.
12 S. Beigoli, A. Hekmat, F. Farzanegan and M. Darroudi, Sol-gel synthesis of amorphous calcium phosphate nanoparticles in brown rice substrate and assessment of their cytotoxicity and antimicrobial activities, *Avicenna J. Phytomed.*, 2022, **12**, 77–88.
13 H. Pan, X. Y. Liu, R. Tang and H. Y. Xu, Mystery of the transformation from amorphous calcium phosphate to hydroxyapatite, *Chem. Commun.*, 2010, **46**, 7415–7417.
14 P. Wolint, L. Näf, D. Schibler, N. Hild, W. J. Stark, P. Giovanoli, M. Calcagni and J. Buschmann, Suspension of amorphous calcium phosphate nanoparticles impact commitment of human adipose-derived stem cells in vitro, *Biology*, 2021, **10**, 675.
15 O. Gröninger, S. Hess, D. Mohn, E. Schneider, W. Stark, S. Märsmann, P. Wolint, M. Calcagni, P. Cinelli and J. Buschmann, Directing stem cell commitment by amorphous calcium phosphate nanoparticles incorporated in PLGA: Relevance of the free calcium ion concentration, *Int. J. Mol. Sci.*, 2020, **21**, 2627.
16 V. Tsikourkitoudi, J. Karlsson, P. Merkl, E. Loh, B. Henriques-Normark and G. A. Sotiriou, Flame-made calcium phosphate nanoparticles with high drug loading for delivery of biologics, *Molecules*, 2020, **25**, 1747.
17 M. Simmler, M. Meier and H. Nirschl, Characterization of Fractal Structures by Spray Flame Synthesis Using X-ray Scattering, *Materials*, 2022, **15**, 2124.
18 W. Wang, X. Zhou, H. Wang, G. Zhou and X. Yu, Fabrication and Evaluation of PCL/PLGA/β-TCP Spiral-Structured Scaffolds for Bone Tissue Engineering, *Bioengineering*, 2024, **11**, 732.
19 M. Herrero-Herrero, J. A. Gómez-Tejedor and A. Vallés-Lluch, Role of Electrospinning Parameters on Poly(Lactic-co-Glycolic Acid) and Poly(Caprolactone-co-Glycolic acid) Membranes, *Polymers*, 2021, **13**, 695.
20 F. Sun, X. Sun, H. Wang, C. Li, Y. Zhao, J. Tian and Y. Lin, Application of 3D-Printed, PLGA-Based Scaffolds in Bone Tissue Engineering, *Int. J. Mol. Sci.*, 2022, **23**, 5831.
21 F. A. Sheikh, H. W. Ju, B. M. Moon, O. J. Lee, J.-H. Kim, H. J. Park, D. W. Kim, D.-K. Kim, J. E. Jang, G. Khang and C. H. Park, Hybrid scaffolds based on PLGA and silk for bone tissue engineering, *J. Tissue Eng. Regener. Med.*, 2016, **10**, 209–221.
22 M. Bensharada, R. Telford, B. Stern and V. Gaffney, Loss on ignition vs. thermogravimetric analysis: a comparative study to determine organic matter and carbonate content in sediments, *J. Paleolimnol.*, 2022, **67**, 191–197.
23 H. A. Sturges, The Choice of a Class Interval, *J. Am. Stat. Assoc.*, 1926, **21**, 65–66.
24 E. Batoni, N. N. Tavernaraki, V. Platania, C. De Maria, M. Chatzinikolaidou and G. Vozzi, 3D printed osteoporotic bone model validated in dynamic culture, *Bioprinting*, 2025, **48**, e00410.
25 F. J. Geissel, V. Platania, N. DeBerardinis, C. Skjöldebrand, G. N. Belibasakis, C. Persson, G. Hulsart-Billström, M. Chatzinikolaidou and G. A. Sotiriou, Nanostructured Ag–Bioglass Implant Coatings with Antibacterial and

 This journal is © The Royal Society of Chemistry 2025

Open Access Article. Published on 29 2025. Downloaded on 2025/12/20 04:03:16.
This article is licensed under a Creative Commons Attribution 3.0 Unported Licence.

Osteogenic Activity, *Adv. Mater. Interfaces*, 2023, **10**, 2201980.

26 L. Mädler, H. K. Kammler, R. Mueller and S. E. Pratsinis, Controlled synthesis of nanostructured particles by flame spray pyrolysis, *J. Aerosol Sci.*, 2002, **33**, 369–389.

27 S. Ataol, A. Tezcaner, O. Duygulu, D. Keskin and N. E. Machin, Synthesis and characterization of nanosized calcium phosphates by flame spray pyrolysis, and their effect on osteogenic differentiation of stem cells, *J. Nanopart. Res.*, 2015, **17**, 95.

28 S. Loher, W. J. Stark, M. Maciejewski, A. Baiker, S. E. Pratsinis, D. Reichardt, F. Maspero, F. Krumeich and D. Günther, Fluoro-apatite and Calcium Phosphate Nanoparticles by Flame Synthesis, *Chem. Mater.*, 2005, **17**, 36–42.

29 P. Merkl, M.-S. Aschtgen, B. Henriques-Normark and G. A. Sotiriou, Biofilm interfacial acidity evaluation by pH-Responsive luminescent nanoparticle films, *Biosens. Bioelectron.*, 2021, **171**, 112732.

30 I. Erceg, J. Kontrec, V. Strasser, A. Selmani, D. Domazet Jurašin, M. Ćurlin, B. N. Džakula, N. Matijaković Mlinarić, S. Šegota, D. M. Lyons, D. Kralj and M. D. Sikirić, Precipitation of Calcium Phosphates and Calcium Carbonates in the Presence of Differently Charged Liposomes, *Minerals*, 2022, **12**, 208.

31 P. J. M. Smeets, K. R. Cho, R. G. E. Kempen, N. A. J. M. Sommerdijk and J. J. De Yoreo, Calcium carbonate nucleation driven by ion binding in a biomimetic matrix revealed by in situ electron microscopy, *Nat. Mater.*, 2015, **14**, 394–399.

32 X. Wang, J. Yang, C. M. Andrei, L. Soleymani and K. Grandfield, Biomineralization of calcium phosphate revealed by in situ liquid-phase electron microscopy, *Commun. Chem.*, 2018, **1**, 80.

33 H. Il Ryu, M. S. Koo, S. Kim, S. Kim, Y.-A. Park and S. M. Park, Uniform-thickness electrospun nanofiber mat production system based on real-time thickness measurement, *Sci. Rep.*, 2020, **10**, 20847.

34 P. Korycka, A. Mirek, K. Kramek-Romanowska, M. Grzeczkowicz and D. Lewińska, Effect of electrospinning process variables on the size of polymer fibers and bead-on-string structures established with a 23 factorial design., *Beilstein J. Nanotechnol.*, 2018, **9**, 2466–2478.

35 J. K. Hong, J. Y. Bang, G. Xu, J.-H. Lee, Y.-J. Kim, H.-J. Lee, H. S. Kim and S.-M. Kwon, Thickness-controllable electrospun fibers promote tubular structure formation by endothelial progenitor cells., *Int. J. Nanomed.*, 2015, **10**, 1189–1200.

36 K. Loukelis, D. Papadogianni, J. E. Kruse and M. Chatzinikolaidou, The effects of gellan gum concentration on electrospinning and degradation of flexible, crosslinker-free scaffolds for bone tissue engineering, *Carbohydr. Polym. Technol. Appl.*, 2024, **7**, 100454.

37 D. De Cicco, Z. Asaee and F. Taheri, Use of Nanoparticles for Enhancing the Interlaminar Properties of Fiber-Reinforced Composites and Adhesively Bonded Joints—A Review, *Nanomaterials*, 2017, **7**, 360.

38 R. Olivares-Navarrete, E. M. Lee, K. Smith, S. L. Hyzy, M. Doroudi, J. K. Williams, K. Gall, B. D. Boyan and Z. Schwartz, Substrate Stiffness Controls Osteoblastic and Chondrocytic Differentiation of Mesenchymal Stem Cells without Exogenous Stimuli, *PLoS One*, 2017, **12**, e0170312.

39 M. Sun, G. Chi, J. Xu, Y. Tan, J. Xu, S. Lv, Z. Xu, Y. Xia, L. Li and Y. Li, Extracellular matrix stiffness controls osteogenic differentiation of mesenchymal stem cells mediated by integrin α5, *Stem Cell Res. Ther.*, 2018, **9**, 52.

40 L. D. Quarles, D. A. Yohay, L. W. Lever, R. Caton and R. J. Wenstrup, Distinct proliferative and differentiated stages of murine MC3T3-E1 cells in culture: An in vitro model of osteoblast development, *J. Bone Miner. Res.*, 1992, **7**, 683–692.

41 M. F. Abazari, Z. Hosseini, S. Zare Karizi, S. Norouzi, M. Amini Faskhoudi, E. Saburi, S. E. Enderami, A. Ardeshirylajimi and H. Mohajerani, Different osteogenic differentiation potential of mesenchymal stem cells on three different polymeric substrates, *Gene*, 2020, **740**, 144534.

42 D. S. Amarasekara, S. Kim and J. Rho, Regulation of Osteoblast Differentiation by Cytokine Networks, *Int. J. Mol. Sci.*, 2021, **22**, 2851.

43 D. W. Hutmacher, J. T. Schantz, C. X. F. Lam, K. C. Tan and T. C. Lim, State of the art and future directions of scaffold-based bone engineering from a biomaterials perspective., *J. Tissue Eng. Regener. Med.*, 2007, **1**, 245–260.

44 H. Zhou and J. Lee, Nanoscale hydroxyapatite particles for bone tissue engineering, *Acta Biomater.*, 2011, **7**, 2769–2781.

45 Q. Hu, Z. Tan, Y. Liu, J. Tao, Y. Cai, M. Zhang, H. Pan, X. Xu and R. Tang, Effect of crystallinity of calcium phosphate nanoparticles on adhesion, proliferation, and differentiation of bone marrow mesenchymal stem cells, *J. Mater. Chem.*, 2007, **17**, 4690.

46 P. J. ter Brugge, J. G. C. Wolke and J. A. Jansen, Effect of calcium phosphate coating crystallinity and implant surface roughness on differentiation of rat bone marrow cells, *J. Biomed. Mater. Res.*, 2002, **60**, 70–78.